JOURNAL OF THE AMERICAN CHEMICAL SOCIETY

Article

pubs.acs.org/JACS

# $(Sr_{1-x}Ba_x)FeO_2$ ($0.4 \leq x \leq 1$): A New Oxygen-Deficient Perovskite Structure

Takafumi Yamamoto,[†,‡] Yoji Kobayashi,[†] Naoaki Hayashi,[§] Cédric Tassel,[†,∥] Takashi Saito,[⊥] Shoji Yamanaka,[#] Mikio Takano,[∇] Kenji Ohoyama,[○] Yuichi Shimakawa,[⊥,◆] Kazuyoshi Yoshimura,[‡] and Hiroshi Kageyama*,[†,‡,∇,◆]

[†]Department of Energy and Hydrocarbon Chemistry, Graduate School of Engineering, Kyoto University, Kyoto 615-8510, Japan

[‡]Department of Chemistry, Graduate School of Science, Kyoto University, Kyoto 606-8502, Japan

[§]Micro/Nano Fabrication Hub, Center for the Promotion of Interdisciplinary Education and Research, Kyoto University, Yoshida-Honmachi, Sakyo, Kyoto 606-8501, Japan

[∥]The Hakubi Center for Advanced Research, Kyoto University, Yoshida-Ushinomiya-cho, Sakyo-ku, Kyoto 606-8302, Japan

[⊥]Institute for Chemical Research, Kyoto University, Kyoto 611-0011, Japan

[#]Department of Applied Chemistry, Graduate School of Engineering, Hiroshima University, Higashi-Hiroshima 739-8527, Japan

[∇]Institute for Integrated Cell-Material Sciences, Kyoto University, Kyoto 606-8501, Japan

[○]Institute for Materials Research, Tohoku University, 2-1-1 Katahira, Aoba-ku, Sendai 980-8577, Japan

[◆]CREST, Japan Science and Technology Agency (JST), Kawaguchi Center Building 4-1-8, Honcho, Kawaguchi, Saitama 332-0012, Japan

*Supporting Information*

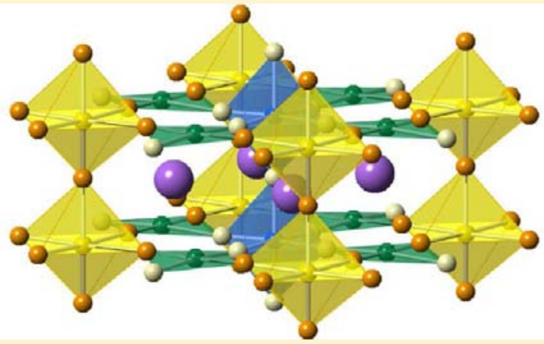

**ABSTRACT:** Topochemical reduction of (layered) perovskite iron oxides with metal hydrides has so far yielded stoichiometric compositions with ordered oxygen defects with iron solely in $FeO_4$ square planar coordination. Using this method, we have successfully obtained a new oxygen-deficient perovskite, $(Sr_{1-x}Ba_x)FeO_2$ ($0.4 \leq x \leq 1.0$), revealing that square planar coordination can coexist with other 3−6-fold coordination geometries. This $BaFeO_2$ structure is analogous to the $LaNiO_{2.5}$ structure in that one-dimensional octahedral chains are linked by planar units, but differs in that one of the octahedral chains contains a significant amount of oxygen vacancies and that all the iron ions are exclusively divalent in the high-spin state. Mössbauer spectroscopy demonstrates, despite the presence of partial oxygen occupations and structural disorders, that the planar-coordinate $Fe^{2+}$ ions are bonded highly covalently, which accounts for the formation of the unique structure. At the same time, a rigid 3D Fe−O−Fe framework contributes to structural stabilization. Powder neutron diffraction measurements revealed a *G*-type magnetic order with a drastic decrease of the Néel temperature compared to that of $SrFeO_2$, presumably due to the effect of oxygen disorder/defects. We also performed La substitution at the Ba site and found that the oxygen vacancies act as a flexible sink to accommodate heterovalent doping without changing the Fe oxidation and spin state, demonstrating the robustness of this new structure against cation substitution.

## 1. INTRODUCTION

Perovskite $ABO_3$ (Figure 1a) and spinel $AB_2O_4$ oxides represent two major classes in crystalline complex metal oxides and are known to exhibit exotic properties such as giant magnetoresistance, high-$T_c$ superconductivity, metal−insulator transitions, and fast ion conductivity.[1−10] The rich diversity of chemical and physical properties in both structures is derived from their ability to accommodate various metal elements at both the A and B sites with a wide range of ionic radius and valence. Another characteristic, often found in the perovskite structure but rarely in the spinel structure, is the high tolerance for oxygen nonstoichiometry. For example, annealing a wide-gap insulator, $SrTiO_3$, in a reducing atmosphere introduces a small amount of oxygen vacancies (i.e., electron doping), which eventually lead to superconductivity at low temperatures.[11] Proton conductivity arises from the creation of a large amount of oxygen vacancies by aliovalent A or B site substitution as found in $Sr(Zr_{1-\delta}Y_\delta)O_{3-\delta/2}$ in a wet atmosphere.[12]

**Received:** January 23, 2012
**Published:** June 18, 2012

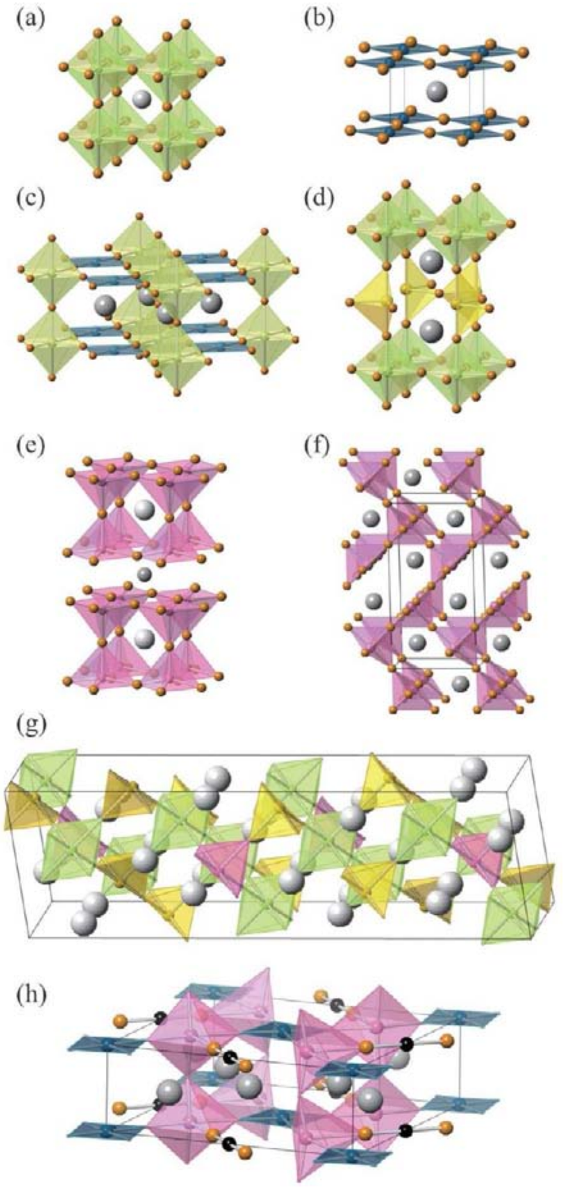

**Figure 1.** Structures of perovskite $ABO_3$ and perovskite $ABO_{3-\delta}$ with ordered oxygen vacancies: perovskite $ABO_3$ with octahedra (a), infinite-layer $ABO_2$ ($\delta = 1$) with square planes (b). Various $ABO_{2.5}$ ($\delta = 0.5$) structures are shown in (c)−(g): $LaNiO_{2.5}$ with octahedra and square planes (c), brownmillerite $ABO_{2.5}$ with octahedra and tetrahedra (d), $YBaCoO_{2.5}$ with pyramids (e), $CaMnO_{2.5}$ with pyramids (f), $BaFeO_{2.5}$ with octahedra, pyramids, and tetrahedra (g). The $(La,Sr)CuO_2$ structure is shown in (h). White and gray spheres represent A site cations. B site cations lie in the center of the polyhedra, and black spheres in (h) represent two-coordinate copper ions.

When the oxygen vacancy level in a perovskite ($\delta$ in $ABO_{3-\delta}$) is commensurate with respect to the underlying lattice, various types of oxygen vacancy order occur, often accompanied by breaking of translational symmetry, which is analogous to the metal−insulator (Mott) transition in electron systems.[13] Such order in oxygen vacancies has been typically observed when $\delta$ = 0.125 ($SrFeO_{2.875}$),[14] $\delta$ = 0.2 ($CaVO_{2.8}$),[15] $\delta$ = 0.25 ($SrFeO_{2.75}$, $Y_{1/2}Ba_{1/2}CoO_{2.75}$),[14,16] and $\delta$ = 0.4 ($SrMnO_{2.6}$).[17] Among them, $\delta$ = 0.5 ($ABO_{2.5}$) is a nexus of a number of structures with ordered oxygen vacancies. The brownmillerite structure, for example, $SrCoO_{2.5}$, known as a low-temperature oxide conductor, consists of alternate stacks of $CoO_4$ tetrahedral layers and $CoO_6$ octahedral layers (Figure 1d).[18] The $LaNiO_{2.5}$ structure contains corner-shared $NiO_6$ octahedral chains along the tetragonal *c* axis that are linked by $NiO_4$ square planes (Figure 1c).[19,20] $(Y_{1/2}Ba_{1/2})CoO_{2.5}$ and $CaMnO_{2.5}$ consist only of $BO_5$ pyramids, but differ in that the former forms oxygen vacancy layers as a result of $Y^{3+}/Ba^{2+}$ order along the *c* axis (Figure 1e),[21] while the latter forms one-dimensional vacancy channels (Figure 1f).[17,22] The $BaFeO_{2.5}$ structure contains three kinds of Fe coordination geometries, octahedra, pyramids, and tetrahedra (Figure 1g).[23]

The infinite-layer (IL) structure $ABO_2$ ($\delta$ = 1; Figure 1b) is the most oxygen-deficient perovskite, where, relative to $ABO_3$, the apical oxygen atoms are completely removed to form $BO_4$ square planar coordination. $SrCuO_2$,[24] $LaNiO_2$,[25] and $SrFeO_2$[26] adopt this structure. Among these, $SrCuO_2$ was investigated intensively, exploiting high-pressure synthesis to electron-dope by lanthanide substitution[27,28] and to apply chemical pressure by Ba or Ca substitution for Sr.[24] The formation of $LaNiO_2$ is naturally understood because $Ni^+$ has the same $d^9$ electronic configurations as $Cu^{2+}$ with a half-filled $d_{x^2-y^2}$ orbital that favors square planar geometry. Though not Jahn−Teller active, $Fe^{2+}$ ($d^6$) ions in $SrFeO_2$, prepared through a low-temperature $CaH_2$ reduction, bear square planar coordination. Interestingly, owing to the highly covalent nature in Fe−O interactions, this iron oxide can tolerate a large amount of A site substitution; Ba-for-Sr substitution is possible up to 30%.[29] With Ca, the ideal IL structure remains up to 80%, beyond which the $FeO_4$ square planes become slightly distorted toward tetrahedra together with coherent rotation, providing a distorted IL structure.[30,31] Other than the IL structure, the so-called 8−8−16 structure, $(La,Sr)CuO_2$ with two-, four-, and five-coordinated copper, was reported for $\delta$ = 1 (Figure 1h).[32]

Given iron's abundance and low toxicity, exploring novel iron oxides is a significant issue. The series of square planar coordinate iron oxides such as $SrFeO_2$,[24] $Sr_3Fe_2O_5$,[33] and $Sr_3Fe_2O_4Cl_2$[34] is appealing because of their interesting properties, including a high Néel temperature (473 K) in $SrFeO_2$, pressure-induced transitions (a spin-state transition, an insulator-to-metal transition, and an antiferromagnetic-to-ferromagnetic transition) in $SrFeO_2$[35] and $Sr_3Fe_2O_5$,[36] and a nontrivial spin structure in $Sr(Fe,Mn)O_2$.[37] These properties originate from extremely strong covalent interactions of $Fe^{2+}$ ions in square planar coordination, as revealed by a small isomer shift (<0.5 mm/s) in the Mössbauer spectroscopy.[24] Such covalent interactions should be important for applications that work at high temperatures. However, all the reported square planar coordinate iron oxides have been exclusively composed of a single iron site,[26,29,31,33,34,38] thereby limiting variations in terms of Fe−O extended networks.

Compared to a conventional $H_2$ gas reaction,[39,40] a low-temperature reduction by metal hydrides ($CaH_2$, NaH, LiH) is a useful method to introduce more oxygen vacancies in transition-metal oxides.[41−43] The reducing power of these metal hydrides is strong even at low temperatures (<500 °C), while the use of low temperature helps the reaction to proceed topochemically. In this study, we report a novel oxygen vacancy ordered perovskite structure with the $ABO_2$ composition. The topochemical low-temperature synthesis and the chemical and structural characterization of $(Sr_{1-x}Ba_x)FeO_2$ ($0 \leq x \leq 1.0$) are presented. It was previously demonstrated that $(Sr_{1-x}Ba_x)FeO_2$ for $0 \leq x \leq 0.3$ crystallizes in the ideal IL structure.[29] However, we found here that additional Ba substitution induces a first-order structural transition involving a large, discontinuous lattice expansion. The resulting new structure is an oxygen-deficient perovskite related in part to the $LaNiO_{2.5}$ structure, but with extensive oxygen defects and disorder (thus with various coordination geometries). The magnetic properties and the effect of aliovalent A site substitution ascribed, in part, to the flexible oxygen composition in this structural framework are demonstrated.

## 2. EXPERIMENTAL PROCEDURE

Precursor materials $(Sr_{1-x}Ba_x)FeO_{3-\delta}$ ($x$ = 0.4, 0.5, 0.6, 0.7, 0.8, 0.9 and 1.0; $\delta \leq 0.5$) were prepared by mixing stoichiometric amounts of $SrCO_3$ (99.99%), $BaCO_3$ (99.99%), and $Fe_2O_3$ (99.99%), pelletizing, and heating at 1473 K in air for 48 h with one intermediate grinding. For $x$ = 0.9 and 1.0, the heat treatment in air led to a hexagonal perovskite phase, $(Sr,Ba)Fe^{4+}O_3$, as reported.[44] We prevented formation of the hexagonal phase by heating the mixture in a reducing atmosphere to stabilize a phase with a lower iron valence; we successfully obtained a monoclinic phase $(Sr,Ba)Fe^{3+}O_{2.5}$ by heating at 1273 K for 24 h in flowing nitrogen with one intermediate grinding.[23]

The obtained precursors were ground well with a 2 M excess of $CaH_2$ in an Ar-filled glovebox, sealed in an evacuated Pyrex tube (volume 15 $cm^3$) with a residual pressure of less than $1.3 \times 10^{-8}$ MPa, and reacted under various temperatures and durations as listed in Table 1. The residual $CaH_2$ and the CaO byproduct were removed by washing with an $NH_4Cl$/methanol solution (0.15 mol/L). It is seen from Table 1 that, for $x$ = 0.4−0.9, an annealing temperature higher than 593 K and a reaction time longer than 3 days is required to complete the reaction. Note that $SrFeO_2$ can be prepared at 553 K within 1 day.[26] When $(Sr_{1-x}Ba_x)FeO_{3-\delta}$ ($x$ = 0.5−0.8) were heated with $CaH_2$ at lower temperatures, e.g., 573 K for 3 days, a small amount of a nonreacted $(Sr,Ba)FeO_{2.5}$ phase was obtained together with the new $(Sr,Ba)FeO_2$ phase. For $x$ = 0.4 and 0.9, 14 days of reaction time at 593 K is required to isolate the pure phase.

Table 1. Reaction Conditions for $(Sr_{1-x}Ba_x)FeO_2$

| $x$ | reaction temp (K) | reaction time (days) | reducing agent | obtained phase |
|---|---|---|---|---|
| 0.0[a] | 553 | 1 | $CaH_2$ | IL |
| 0.1, 0.2, 0.3[a] | 553 | 3 | $CaH_2$ | IL |
| 0.4 | 593 | 14 | $CaH_2$ | $BaFeO_2$-type |
| 0.5, 0.6, 0.7, 0.8 | 593 | 3 | $CaH_2$ | $BaFeO_2$-type |
| 0.9 | 593 | 14 | $CaH_2$ | $BaFeO_2$-type |
| 1.0 | 413 | 3 | NaH | $BaFeO_2$-type |

[a] We used the values for $x$ = 0.0−0.3 in previous studies.[26,29]

However, the $CaH_2$ reduction of $BaFeO_{2.5}$ ($x$ = 1) failed in any conditions employed; the precursor decomposed to (Sr,Ba)O and Fe when reacted at 773 K, while no reaction occurred when reacted at 673 K. Consequently, we used NaH as an alternative reductant and obtained the $BaFeO_2$ phase; $BaFeO_{2.5}$ was ground with a 2 M excess of NaH in the Ar-filled glovebox, sealed in the same way, and reacted at 413 K for 3 days. The residual NaH and the NaOH byproduct were removed by washing with methanol.

It was observed that, when kept in air for a week, the $x$ = 0.5, 0.6, 0.7, and 0.8 samples were partially oxidized, while the $x$ = 0.4, 0.9, and 1.0 compositions were much more air sensitive; storage in the Ar-filled glovebox (1 ppm < $[H_2O]$, 1 ppm < $[O_2]$) for several days resulted in oxidization back to $(Sr,Ba)FeO_{2.5}$. It is likely that the average A site radius in the range of $x$ = 0.5−0.8 is accommodated best by the structure.

La substitution at the barium site was attempted with the ultimate motivation to dope electrons to the $Fe^{2+}O_2$ layer and induce metallic conductivity (superconductivity). The oxygen-deficient precursor perovskite $(Ba_{0.8}La_{0.2})FeO_{3-\delta}$ ($\delta$ < 0.5) was prepared by mixing stoichiometric amounts of $La_2O_3$ (99.9%), $BaCO_3$ (99.99%), and $Fe_2O_3$ (99.99%), pelletizing, and heating at 1473 K for 24 h in air. Subsequently, the pellet was ground, pelletized, and heated at 1573 K for 24 h in air. The obtained precursor was ground thoroughly with a 2 M excess of NaH in the Ar-filled glovebox, sealed, and reacted at 443 K for 3 days. The final product, isolated by washing with methanol, was air sensitive as was $BaFeO_2$.

The sample purity of the precursors and final products was checked by X-ray diffraction (XRD) using an M18XHF diffractometer (Mac Science) and a D8 ADVANCE diffractometer (Burker AXS) with Cu K$\alpha$ radiation ($\lambda$ = 1.54056 Å). For structural refinements of $(Sr_{0.2}Ba_{0.8})FeO_2$, the most stable composition, high-resolution synchrotron powder XRD experiments were performed at room temperature using a large Debye−Scherrer camera installed at beamline BL02B2 of the Japan Synchrotron Radiation Research Institute (SPring-8). We used an imaging plate as a detector. Incident beams from a bending magnet were monochromatized to 0.7755 Å. The finely ground powder samples were sieved (32 μm) and put into a Pyrex capillary 0.1 mm in inner diameter. The sealed capillary was rotated during measurements to reduce the effect of the potential preferential orientation.

Powder neutron diffraction experiments on $(Sr_{0.4}Ba_{0.6})FeO_2$ and $(Sr_{0.2}Ba_{0.8})FeO_2$ were carried out on the Kinken powder diffractometer with multicounters for HERMES (high-efficiency and high-resolution measurements) of the Institute for Materials Research, Tohoku University, installed at a guide hall of the JRR-3 reactor in the Japan Atomic Energy Agency (JAEA), Tokai.[45] The incident neutron was monochromatized to 1.82646 Å by the 331 reflection of a vent Ge crystal. A 12′−blank−sample−18′ collimation was employed. A polycrystalline sample of 3 g was placed into a He-filled vanadium cylinder. The sample temperature was controlled from 20 to 298 K. The data were collected with a step scan procedure using 150 $^3He$ tube detectors in the $2\theta$ range from 3° to 153° with a step width of 0.1°.

The obtained synchrotron XRD and neutron diffraction data were analyzed by the Rietveld method using the RIETAN-FP program.[46] The agreement indices used were $R$-weighted pattern, $R_{wp} = [\sum w_i(y_{io} - y_{ic})^2/\sum w_i(y_{io})^2]^{1/2}$, $R$-pattern, $R_p = \sum|y_{io} - y_{ic}|/\sum(y_{io})$, and goodness-of-fit (GOF), $\chi^2 = [R_{wp}/R_{exptl}]^2$, where $R_{exptl} = [(N-P)/\sum w_i y_{io}^2]^{1/2}$, $y_{io}$ and $y_{ic}$ are the observed and calculated intensities, $w_i$ is the weighting factor, $N$ is the total number of $y_{io}$ data when the background is refined, and $P$ is the number of adjusted parameters.

Thermogravimetric (TG) data of the reduced compounds were collected using a TG-DTA 2000S (Bruker AXS). Typically, 50 mg of sample was put into a Pt pan, and $\alpha$-$Al_2O_3$ was used as a reference. The measurements were performed by heating the sample at 10 K/min under a flow of oxygen with a flow rate of 100 mL/min. The samples after the measurements were identified by XRD measurements.

Mössbauer spectra on $(Sr_{1-x}Ba_x)FeO_2$ for $x$ = 0.5, 0.6, 0.7, and 0.8 and the La-substituted sample after the reduction were taken at room temperature in transmission geometry using a $^{57}Co/Rh$ $\gamma$-ray source. The source velocity was calibrated by $\alpha$-Fe as a reference material. The electrical resistivity of the La-substituted sample after the reduction was measured between 210 and 298 K using a two-probe method. The sample was pelletized to a cylinder (6 mm$\varphi$ × 1 mm) and was sealed by a He-filled container. To check the effect of electrodes, the ohmic behavior of the sample was proved in a low-voltage regime. Activation energies were estimated from the temperature dependence of the resistivity above 230 K by Arrhenius plots.

## 3. RESULTS AND DISCUSSION

**3.1. Synthesis and Lattice Evolution.** The formation of the $(Sr,Ba)FeO_{3-\delta}$ precursors ($\delta \leq 0.5$) was confirmed by laboratory XRD (Figure 1S in the Supporting Information). All the diffraction peaks of the precursors ($x \leq 0.8$) were indexed in a pseudocubic unit cell with $a \approx 3.9$ Å (when tiny superreflection peaks were neglected), while those of the precursors ($x = 0.9$ and 1.0) were indexed in a monoclinic superstructure of $Ba_{28}Fe_{28}O_{70}$ ($BaFeO_{2.5}$), consistent with the previous report.[23] No impurity phases were detected for all precursors. The lattice parameters for $x \leq 0.8$ increase with increasing $x$ (Figure 1S), which is consistent with the larger ionic radius of $Ba^{2+}$ (vs $Sr^{2+}$). The nonlinear $x$ dependence of the lattice parameters implies that the oxygen content varies with $x$.

Figure 2a shows the XRD patterns of the $x = 0.3-1.0$ compounds after the hydride reduction. All the profiles are readily indexed on the basis of a tetragonal unit cell. It can be recognized that, relative to the $x = 0.3$ sample crystallizing in the IL structure,[29] the XRD peaks for $x \geq 0.4$ are largely shifted to lower angles. In addition, several additional super-reflections, related to the simple perovskite cell ($a_p \times b_p \times c_p$) by $2a_p \times 2a_p \times c_p$, are observed. No impurity could be found within the experimental resolution.

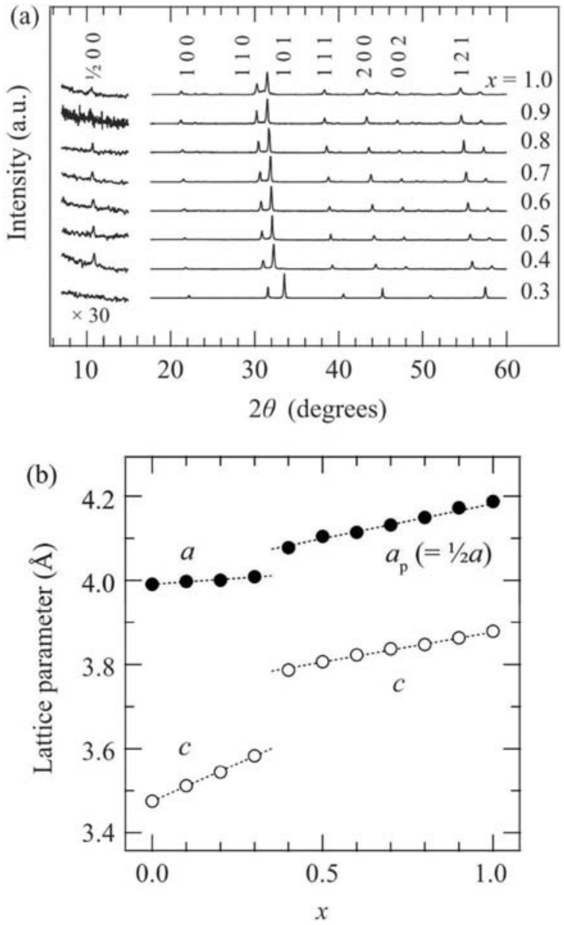

**Figure 2.** (a) XRD patterns of $(Sr_{1-x}Ba_x)FeO_2$ ($0.3 \leq x \leq 1.0$). All patterns could be indexed by a tetragonal system. (b) $a$ (closed) and $c$ (open) parameters of $(Sr_{1-x}Ba_x)FeO_2$ ($0 \leq x \leq 1$). For comparison, the unit cell of the new structure ($0.4 \leq x \leq 1$) is represented as the perovskite cell ($a_p = {}^1/_2 a$). The error bars are within the size of the symbols. The data for $x = 0.0-0.3$ are taken from previous studies.[26,29]

For the sake of comparison, the normalized lattice parameters, $a_p$ ($= a/2$) and $c$, are plotted in the whole $x$ range ($0 \leq x \leq 1$) in Figure 2b and are also presented in Table 1S in the Supporting Information. A prominent jump of the lattice parameters is seen between $x = 0.3$ and $x = 0.4$, strongly indicating a first-order structural phase transition from the IL structure to a new structure with much less density. For $x \geq 0.4$, both crystallographic axes increase linearly with $x$ (Vegard's law), meaning plausibly that, whatever the new structure is, it forms a solid solution and that the oxygen content is unvaried with $x$. The differences in the cell parameters between $x = 0.3$ and 0.4 are 1.7% for $a$ and 5.7% for $c$. The larger increase along the $c$ axis suggests that the new phase of $x \geq 0.4$ contains apical oxygen atoms at least to a certain extent, in contrast to the IL structure where oxygen atoms are exclusively absent at the apical site of the $BO_4$ square plane ($B = Cu^{2+}$, $Ni^+$, $Fe^{2+}$). For $x \leq 0.3$, the $c$ axis increases more steeply than the $a$ axis with $x$ ($\Delta c(Å) = 0.36\Delta x$ vs $\Delta a(Å) = 0.06\Delta x$), reflecting the two-dimensional nature of the IL structure. On the other hand, the lattice evolution for $0.4 \leq x$ is given by $\Delta a$ (Å) $= 0.18\Delta x$ and $\Delta c(Å) = 0.15\Delta x$, indicating that the new structure is likely to be three-dimensional.

As mentioned above, the linear increase of the lattice parameters for $x \geq 0.4$ suggests a constant oxygen content. The TG measurement was carried out to quantify the oxygen stoichiometry. The $x = 0.8$ sample was chosen for this experiment because of its superior chemical stability. As shown in Figure 3, a double weight increase separated by a plateau was observed. A very similar behavior was obtained previously in $SrFeO_2$, $(Sr_{0.8}Ca_{0.2})FeO_2$, and $(Sr_{0.8}Ba_{0.2})FeO_2$.[29] The XRD inspection after rapid quenching of the TG furnace revealed that the plateau in Figure 3 corresponds to the $(Sr_{0.2}Ba_{0.8})FeO_{2.5}$ phase with the monoclinic $BaFeO_{2.5}$ structure,[23] and this phase is, upon further heating, oxidized to the pseudocubic oxygen-deficient perovskite $(Sr_{0.2}Ba_{0.8})FeO_{3-\delta}$ ($\delta < 0.5$). Supposing the oxygen content at the plateau is 2.5, that of the initial phase can be calculated as 2.0. Thus, the chemical formula of the new phase ($x \geq 0.4$) as well as the IL phase ($x \leq 0.3$) can be defined as $(Sr_{1-x}Ba_x)FeO_2$. Moreover, the facile oxidation of $(Sr_{0.2}Ba_{0.8})FeO_2$ to $(Sr_{0.2}Ba_{0.8})FeO_{2.5}$ and $(Sr_{0.2}Ba_{0.8})FeO_{3-\delta}$ ($\delta < 0.5$) at low temperatures (<600 K),

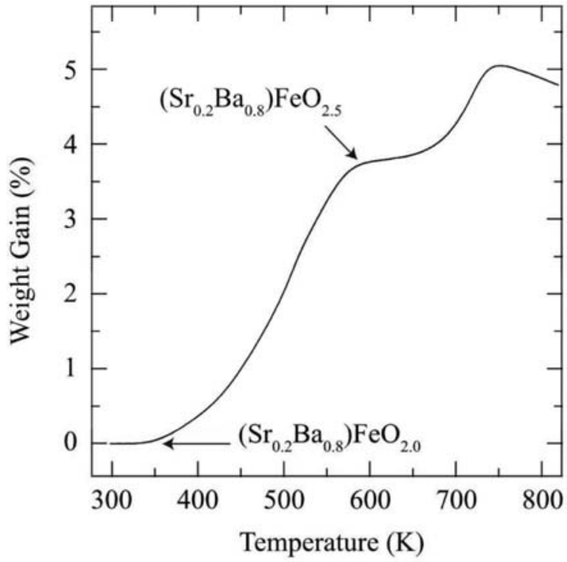

**Figure 3.** Oxidation behavior of $(Sr_{0.2}Ba_{0.8})FeO_2$ ($x = 0.8$) under a flow of oxygen gas.

and vice versa, suggests a topochemical conversion; namely, the new phase is structurally related to the perovskite structure.

**3.2. Structural Refinements.** The structural refinement of synchrotron XRD and neutron diffraction was performed for $x = 0.8$. This composition was selected because of the highest chemical stability and also because of the highest crystallinity revealed by the laboratory XRD experiments. Shown in Figure 4a is the synchrotron XRD pattern, which could be indexed on a tetragonal $2a_p \times 2a_p \times c_p$ cell, with $a = 8.302$ Å and $c = 3.845$ Å, consistent with the laboratory XRD data. No systematic extinct reflections were present. From this, one can derive possible tetragonal space groups as $P4/mmm$, $P\bar{4}2m$, $P\bar{4}m2$, $P4mm$, $P422$, $P4/m$, $P\bar{4}$, and $P4$. There are several unindexed peaks at 9.1°, 14.7°, and 18.7° (with intensities of less than 0.5% of that of the main peak), which could not be assigned by assuming a lowered symmetry or a superstructure. Thus, they come from tiny impurity phases. We initially built a structural model on the basis of the IL structure (space group $P4/mmm$), but using the $2a_p \times 2a_p \times c_p$ cell. The A site was placed at $(x, x, 1/2)$, where 20% Sr and 80% Ba atoms are randomly distributed. Three Fe atoms were placed at $1a$ (0, 0, 0), $1c$ (1/2, 1/2, 0), and $2f$ (0, 1/2, 0) and two O atoms at $4l$ $(x, 0, 0)$ and $4n$ $(x, 1/2, 0)$. Here, all the variable atomic coordinates were initially set as 1/4. This IL-derivative model resulted in a rather poor agreement at its best with $\chi^2 = 16.48$.

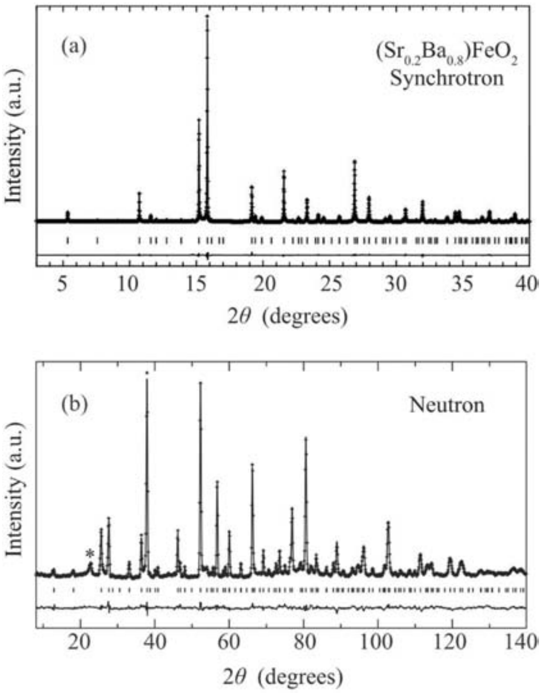

**Figure 4.** (a) Structural characterization of $(Sr_{0.2}Ba_{0.8})FeO_2$ by Rietveld refinement of synchrotron XRD data at room temperature with $\lambda = 0.7755$ Å ($R_p = 3.17\%$, $R_{wp} = 4.73\%$, $\chi^2 = 4.14$, $R_I = 2.20\%$, $R_F = 1.73\%$) and (b) that of neutron diffraction data at room temperature with $\lambda = 1.82646$ Å ($R_p = 4.43\%$, $R_{wp} = 5.63\%$, $\chi^2 = 2.94$, $R_I = 5.46\%$, $R_F = 3.56\%$). The overlying plus signs and the solid lines represent the observed intensities and the calculated intensities. The bottom solid lines represent the residual intensities. The ticks correspond to the position of the calculated Bragg peaks of the main phase $(Sr_{0.2}Ba_{0.8})FeO_2$. The asterisk in (b) corresponds to a short-range magnetic reflection of $(Sr_{0.2}Ba_{0.8})FeO_2$, which was included as the background of the refinement.

Accordingly, as a next step, the symmetry was lowered to the maximum nonisomorphic subspace groups for $P4/mmm$, that is, $P\bar{4}2m$, $P\bar{4}m2$, $P4mm$, $P422$, and $P4/m$. Among them $P4mm$ led to the best result, but the agreement factors were still poor ($\chi^2$ values never became better than 15.5). $P4$ and $P\bar{4}$, the maximum nonisomorphic subspace groups, respectively, for $P4mm$, $P422$, and $P4/m$ and for $P\bar{4}2m$, $P\bar{4}m2$, and $P4/m$ did not improve the result as well. These results indicate that the real structure deviates significantly from the IL model assumed here.

To find a clue to reach a proper structural model, maximum entropy method (MEM) analysis was carried out by using the model with the $P4/mmm$ space group. Figure 2S in the Supporting Information clearly demonstrates the presence of finite electron density at the apical sites of the square planar iron center. This indicates that the new structure indeed contains apical oxygen atoms, unlike the IL structure. Note that the $c$ axis shows a prominent jump ($\Delta c \approx 0.20$ Å) upon the structural transition when going from the IL phase to the new phase (Figure 2b). This observation also supports a model in which the apical oxygen sites are occupied, at least to a certain extent. Consequently, we decided to start from a model with apical oxygen atoms. Namely, O(3) on $1b$ (0, 0, 1/2), O(4) on $1d$ (1/2, 1/2, 1/2), and O(5) on $2e$ (1/2, 0, 1/2) were added as the apical sites to the IL model. When the occupancy factors ($g$) of the oxygen sites were allowed to move, the $g$ value for O(5) always became close to zero, so it was fixed at zero in consequent refinements. On the other hand, the $g$ values for O(1) and O(3) became close to 1 within the error, so they were fixed at unity. It was conversely observed that the $g$ values for O(2) and O(4) were reduced to ~0.6. Up to this point, we did not put any constraint on the total oxygen content. However, this analysis led to the total oxygen content being close to 2, in reasonable agreement with that obtained from the TG measurements (Figure 3). In addition, this model drastically improved the refinement with $\chi^2 = 8.14$.

Although the model involving apical oxygen sites led to a much better refinement, several atomic displacement parameters were relatively high, e.g., $U_{iso} \approx 0.03$ Å$^2$ for Fe(2), $U_{iso} \approx 0.05$ Å$^2$ for Fe(3), and $U_{iso} \approx 0.2$ Å$^2$ for O(4). Since one vacancy at the O(2) site creates an $Fe(2)O_3$ coordination environment, Fe(2) would move away from the vacancy. Thus, the three-coordinate iron atom, Fe(2)′, was placed at $4n$ $(x, 1/2, 0)$, while the four-coordinate Fe(2) remained at the more symmetric $2f$ (0, 1/2, 0). This attempt gave $x \approx 0.042$ for Fe(2)′, and reasonably small atomic displacement parameters of $U_{iso} < 0.01$ Å$^2$ were obtained for Fe(2) and Fe(2)′. In contrast, we could not reduce the $U$ values of the Fe(3) and the O(4) sites by introduction of site disorder nor superstructure along the $c$ axis. Therefore, anisotropic displacement parameters $U_{ij}$ were used for these sites, and highly anisotropic displacements were obtained; the Fe(3) atom is displaced along the $c$ axis and the O(4) atom both along the $c$ axis and the $ab$ plane.

To check this proposed structure, and in particular to obtain more precise information on the oxygen positions and their site occupancies, we performed Rietveld refinement using powder neutron diffraction data of the same compound, $(Sr_{0.2}Ba_{0.8})FeO_2$ (see Figure 4b). Like the synchrotron XRD pattern, the neutron diffraction pattern at room temperature could be indexed on a tetragonal $2a_p \times 2a_p \times c_p$ cell. Note that tiny peaks at 9.5° and 43.7° result from unknown impurity phases. We started the refinement with the final model obtained from the synchrotron XRD data. During the refinement, the atomic parameters of the O atoms, including occupancy factors, were

Table 2. Crystallographic Data for $(Sr_{0.2}Ba_{0.8})FeO_2$ ($Z = 4$)[a]

| atom | site | occupancy ($g$) | $x$ | $y$ | $z$ | $U_{iso}$/Å$^2$ | $U_{11}$/Å$^2$ = $U_{22}$/Å$^2$ | $U_{33}$/Å$^2$ |
|---|---|---|---|---|---|---|---|---|
| Sr(1) | 4*k* | 0.2 | 0.23667(3) | 0.23667(3) | 0.5 | 0.0098(1) | | |
| Ba(1) | 4*k* | 0.8 | 0.23667(3) | 0.23667(3) | 0.5 | 0.0098(1) | | |
| Fe(1) | 1*a* | 1 | 0 | 0 | 0 | 0.0106(7) | | |
| Fe(2) | 2*f* | 0.208(6) | 0 | 0.5 | 0 | 0.0078(6) | | |
| Fe(2)′ | 4*n* | 0.396(3) | 0.0421(3) | 0.5 | 0 | 0.0078(6) | | |
| Fe(3) | 1*c* | 1 | 0.5 | 0.5 | 0 | | 0.029(1) | 0.91(3) |
| O(1) | 4*l* | 1 | 0.2833(4) | 0 | 0 | 0.023(1) | | |
| O(2) | 4*n* | 0.604(3) | 0.2665(8) | 0.5 | 0 | 0.032(2) | | |
| O(3) | 1*b* | 1 | 0 | 0 | 0.5 | 0.003(1) | | |
| O(4) | 1*d* | 0.583(13) | 0.5 | 0.5 | 0.5 | | 0.29(3) | 0.16(3) |

[a] Space group *P*4/*mmm*; $a = 8.30241(4)$ Å and $c = 3.84506(2)$ Å for synchrotron XRD data, and $a = 8.3017(2)$ Å and $c = 3.84632(9)$ Å for neutron diffraction data.

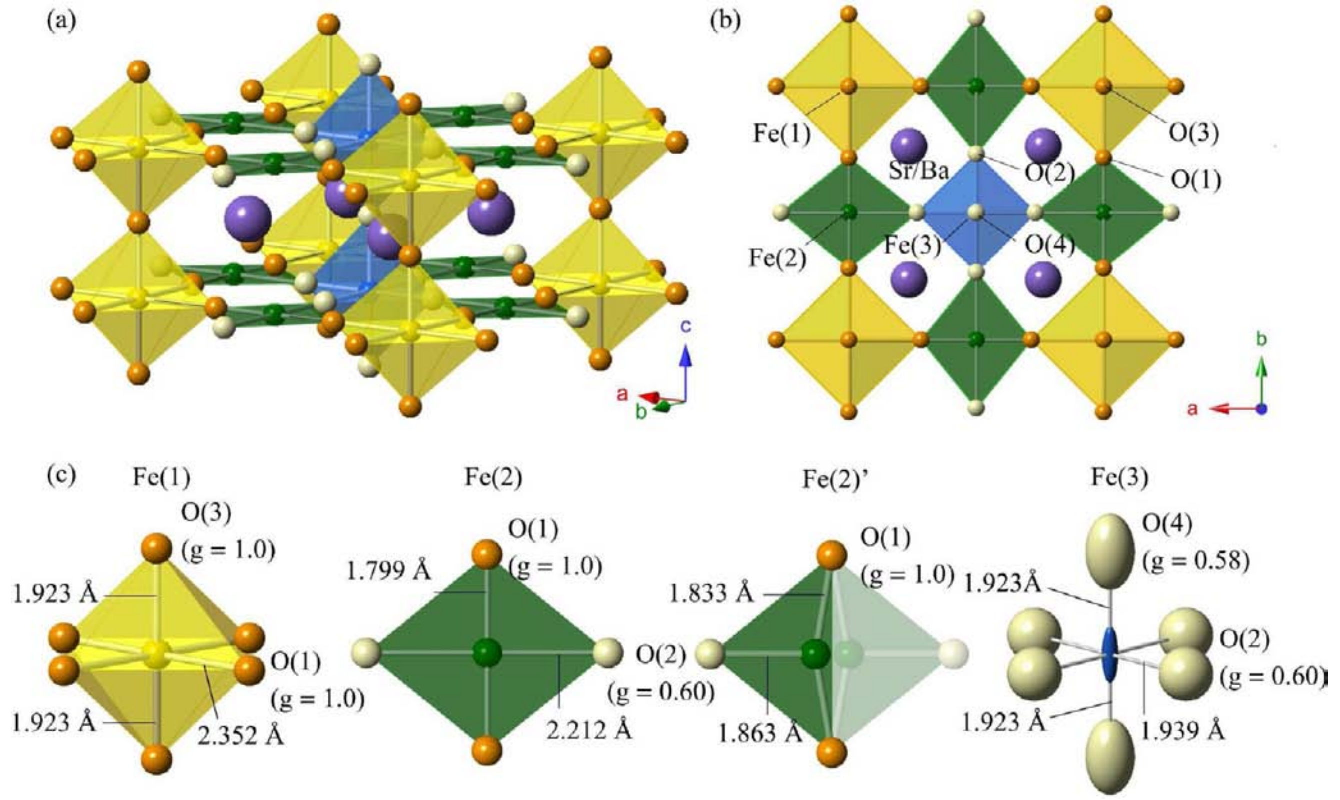

**Figure 5.** Structure of $(Sr_{0.2}Ba_{0.8})FeO_2$. Purple, yellow, green, and blue spheres represent Ba/Sr, Fe(1), Fe(2), and Fe(3) atoms, respectively. Orange spheres represent fully occupied O(1) and O(3) atoms ($g = 1.0$), while dilute yellow spheres represent partially occupied O(2) and O(4) atoms ($g < 1.0$), where $g$ represents the site occupancy factor. (a) Structure of $(Sr_{0.2}Ba_{0.8})FeO_2$. (b) [001] projection. Fe(2)′ is neglected in (a) and (b). (c) Coordination environment around each iron. The displacement ellipsoids are depicted in the coordination environment around Fe(3).

allowed to move, while those of Sr, Ba, and Fe atoms were fixed. Then we returned to the synchrotron XRD data for mainly refining the atomic parameters of the A and Fe atoms, while retaining adjustable parameters of O atoms. After this process was repeated several times, the oxygen content was converged to 2.04(1), which is very close to 2.0 obtained from the TG measurements. Therefore, we decided to fix the oxygen stoichiometry at 2. Agreement parameters for the neutron refinement are $R_p = 3.17\%$, $R_{wp} = 4.73\%$, $\chi^2 = 4.14$, $R_I = 2.20\%$, and $R_F = 1.73\%$ for the synchrotron XRD data and $R_p = 4.43\%$, $R_{wp} = 5.63\%$, $\chi^2 = 2.94$, $R_I = 5.46\%$, and $R_F = 3.56\%$ for the neutron diffraction data. The other space groups with lower symmetry did not lead to better results, and we concluded that *P*4/*mmm* is the most likely space group. The final refinement results are summarized in Table 2, and the structure is represented in Figure 5.

From various experimental observations as addressed above, the compounds in all the range of $0.4 \leq x \leq 1.0$ should be isostructural. Let us call hereafter the refined structure the $BaFeO_2$ structure. The $BaFeO_2$ structure can be described as an "oxygen-deficient" $LaNiO_{2.5}$ structure, which consists of octahedral chains interlinked by square planar units (Figure 1c). However, this similarity does not mean that the $BaFeO_2$ structure was formed by the mere and gradual deintercalation of oxide ions from a $LaNiO_{2.5}$ structure. First, $BaFeO_2$ is a line phase, which means that it has a defined composition and lattice parameters. Upon reduction of $BaFeO_{2.5}$ the oxygen content discontinuously changes from 2.5 and 2 (see Figure 3S, Supporting Information). In addition, the conversion of $BaFeO_2$ from $BaFeO_{2.5}$ ($Ba_{28}Fe_{28}O_{70}$; Figure 1g)[23] involves not only extraction of but also rearrangement of oxide ions. Such a dynamic conversion involving framework rearrangement has also been observed in $SrFeO_2$ (from $SrFeO_{2.5}$), $LaNiO_2$ (from $LaNiO_{2.5}$),[19,20] and $Sr_3Fe_2O_5$ (from $Sr_3FeO_6$).[26,33] Because of the higher reactivity and air sensitivity, $BaFeO_2$ is oxidized back to $BaFeO_{2.5}$ even at room temperature, as in $CaFeO_2$[30] and $Sr_3Fe_2O_5$.[33]

The coordination geometries around iron are illustrated in Figure 5c. There are four iron atoms, Fe(1), Fe(2) × 2, and Fe(3), in the unit cell. Fe(1) resides in a flattened $FeO_6$ octahedron with four long Fe(1)−O(1) bonds (2.352 Å) along the *a* (*b*) axis and two short Fe(1)−O(3) bonds (1.923 Å) along the *c* axis. Bond valence sum (BVS) calculations[47] for Fe(1) gave +1.95. The O(1) site is fully occupied, while the occupancy of the O(2) site is 0.604, meaning that $Fe(2)'O_3$ trigonal planar and $Fe(2)O_4$ rhomboidally distorted square planar coordination geometries are randomly distributed at a rate of 79:21. The four-coordinate Fe(2) has two short Fe(2)−O(1) bonds (1.799 Å) and two long Fe(2)−O(2) bonds (2.212 Å), giving a BVS of +2.23. The three-coordinate Fe(2)′ has two Fe(2)′−O(1) bonds (1.833 Å) and one Fe(2)′−O(2) bond (1.863 Å), giving a BVS of +2.24. This indicates that Fe(2) and Fe(2)′ are also divalent. Fe(3) would have an octahedral coordination if one could neglect the oxygen deficiencies at O(2) and O(4). However, taking the oxygen deficiencies into consideration, the average Fe(3) coordination number is 3.58, implying that the majority of the Fe(3) atoms should be in 3- or 4-fold coordination. The BVS calculations for the three- and four-coordinate Fe(3) gave +1.72 to +1.78 and +2.30 to +2.35, so that this iron site is likely to be divalent. In this way, the three kinds of iron are coordinated quite differently, but they are all divalent, which is once again consistent with the oxygen content of 2.

**3.3. Mössbauer Spectroscopy.** To obtain more insight into local geometries around iron, $^{57}Fe$ Mössbauer spectra were collected for $x = 0.5$, 0.6, 0.7, and 0.8 at room temperature (Figure 6a; Figure 4S, Supporting Information). $BaFeO_2$ ($x = 1.0$) was not measured because of its high air sensitivity. At any concentration measured, the spectrum consists of four sets of paramagnetic doublets, which were well fitted by Lorentzian functions. The results are summarized in Figure 6b and Table 2S in the Supporting Information. All the Mössbauer parameters for $x = 0.5-0.8$ are similar to each other, supporting the successful formation of the new phase as a solid solution.

The black subspectrum has a spectrum weight of 15% and has an isomer shift (IS) of ∼0.35 mm/s, which is a typical value for trivalent iron in a high-spin state. Upon the specimen being cooled below $T_N$, the shape of this doublet did not exhibit any splitting, while other doublets became sextets (not shown), implying that the former does not come from $(Sr_{0.2}Ba_{0.8})FeO_2$. Although no impurity phase was detected by laboratory XRD studies, it probably arises from a trivalent iron-containing paramagnetic amorphous impurity. It is probably formed by over-reduction and decomposition during the hydride reduction and then oxidation to Fe(III) upon exposure to air. We note that the relative subspectrum area derived from the amorphous impurity increased when a more severe reducing condition was employed (e.g., increased reaction temperature). Such an amorphous impurity phase was also observed in the Mössbauer spectra of $(Sr,Ca)FeO_2$ and $(Sr_{1-x}Ba_x)FeO_2$ ($x \leq 0.3$).[29,31] Note that the Mössbauer specimen is different from that used for the TG measurement in Figure 3; when the impurity is ignored, the TG data for the Mössbauer specimen give an oxygen content of 2.1 (Figure 5S, Supporting Information), reasonably consistent with the existence of an Fe(III) impurity phase of such an amount.

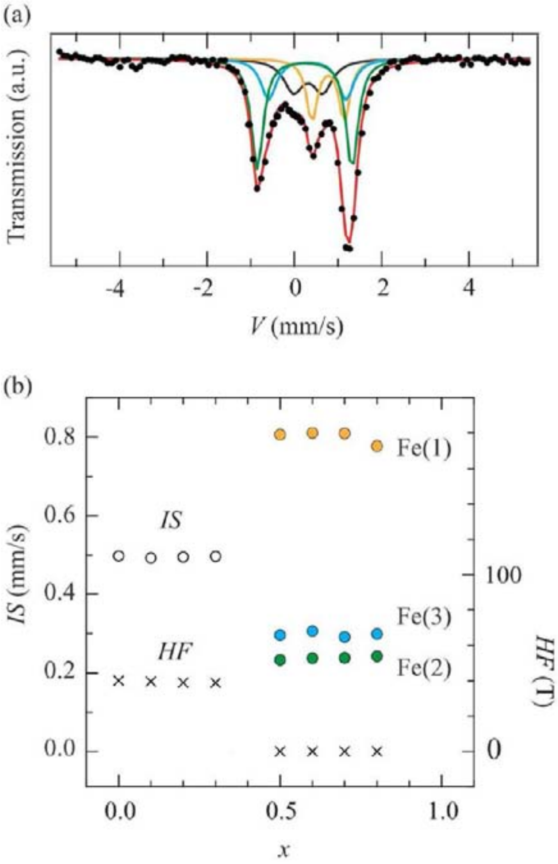

**Figure 6.** (a) Mössbauer spectrum for $x = 0.8$ at room temperature. Circles denote the experimental data. The spectrum was fitted by four components; yellow, green, and blue lines represent subspectra from Fe(1), Fe(2), and Fe(3), respectively. The black line represents an over-reduced, decomposed amorphous impurity formed during the hydride reaction. The red line represents the total fitted spectrum. (b) Hyperfine field (HF) and isomer shift (IS) of $(Sr_{1-x}Ba_x)FeO_2$. The times signs and the open circles represent HF and IS. Closed yellow, green, and blue circles represent IS of Fe(1), Fe(2), and Fe(3), respectively.

The three other Mössbauer subspectra intrinsic to (Sr,Ba)-$FeO_2$ are very consistent with the crystal structure proposed. The spectrum weights for yellow, green, and blue curves in Figure 6a are 22%, 42%, and 21%, respectively. The 1:2:1 ratio of the spectrum weight is what is expected from one Fe(1) ion, two Fe(2) (Fe(2)′) ions, and one Fe(3) ion in the unit cell. It is straightforward to determine which subspectrum corresponds to which iron site. The green subspectrum with the doubled intensity is assigned to Fe(2) and Fe(2)′ in the distorted square planar and trigonal coordination. The yellow subspectrum has a narrow full width at half-maximum (fwhm) of 0.30 mm/s, which is close to the instrumental resolution. This spectrum is thus assigned to the Fe(1) site because the $Fe(1)O_6$ octahedron is free from oxygen defects. The IS value of ∼0.8 mm/s is typical for a divalent high-spin iron in an octahedral environment.[48] The blue subspectrum with a much wider fwhm of 0.42 mm/s is assigned to the Fe(3) site because extensive oxygen defects are present around Fe(3).

We point out again that the new (Sr,Ba)$FeO_2$ compound is a line phase and is reduced (oxidized) discontinuously from (to) (Sr,Ba)$FeO_{2.5}$. It is therefore different from the typical nonstoichiometric oxides, where the oxygen content continuously varies. In such a nonstoichiometric oxide system, more weakly bonded sites are subject to oxygen deficiency. What is observed in (Sr,Ba)$FeO_2$ is, however, opposed to this general trend; despite significant oxygen deficiency, Fe(2) (Fe(2)′) and Fe(3) have smaller IS values of 0.24 and 0.29 mm/s than Fe(1) and typical divalent iron in a high-spin state.[48] Namely, the iron ions with oxygen vacancies in (Sr,Ba)$FeO_2$ are far more covalently bonded.

Fe(2) is in the rhomboidally distorted square planar coordination, and Fe(2)′ is in the trigonal coordination. Therefore, the covalent bonding nature is not limited to the ideal square planar coordination, but is a common nature for iron in planar coordination geometry. To confirm this, we prepared $Sr_3La(Fe,Co)_3O_{7.5}$[43] and performed a Mössbauer experiment to find that the trigonal planar site indeed has a similar value of IS = 0.32 mm/s.

As mentioned above, the majority of Fe(3) atoms should be in 3- and 4-fold coordination. The small IS value of 0.29 mm/s means that Fe(3) is also in planar geometry. If this is so, it is highly possible, despite the absence of long-range vacancy order, that the oxygen vacancies around Fe(3) are not statistically distributed at the octahedral site. Namely, two and three vacancies around a certain Fe(3) atom should *selectively* form, respectively, square planar and trigonal coordination. Such a selective local configuration is reminiscent of the recent work by Attfield et al., who demonstrated a *local* anion order, i.e., *cis*-conformation, of nitrogen atoms in $MO_4N_2$ octahedra in the absence of long-range anionic order.[49]

### 3.4. $BaFeO_2$ Structure.

Although the oxygen content of the reduced materials is unvaried in the whole range of $x$ ($0 \leq x \leq 1$), the $BaFeO_2$ structure differs from the IL structure[24,27,28] and the distorted IL structure $CaFeO_2$,[31] in a number of points. One of the notable features is the ability of square planar coordination to coexist with other coordination polyhedra, giving a three-dimensional extended network. The present result provides a possibility that one can obtain iron oxides with various coordination geometries, including square planes. The deformation from the ideal square plane is also distinct; while the Ca-for-Sr substitution of $SrFeO_2$ beyond the critical concentration (around 80%) leads to a tetrahedral distortion, the Ba-for-Sr substitution for $x \geq 0.4$ leads to a rhomboidal distortion. The strong covalency in $FeO_4$ square planar coordination, as probed by Mössbauer spectroscopy, would permit two types of distortion.

The distortion of $FeO_4$ square planes in the $CaFeO_2$ structure is accounted for by the smaller Ca ion less comfortable in the ideal IL structure, preferring to decrease the coordination number to six from eight.[31] By analogy, the $BaFeO_2$ structure might also be rationalized by the coordination environment around the Ba ion. However, this does not seem to be the case. The BVS of the A site cation in $(Sr_{0.2}Ba_{0.8})FeO_2$ is +1.69, which is smaller than the theoretical value of +2, whereas +2.02 is obtained when a hypothetical IL structure of $(Sr_{0.2}Ba_{0.8})FeO_2$ is assumed, where the lattice parameters are determined by linear extrapolation of the curves in Figure 2b. This fact indicates that the key to stabilizing the $BaFeO_2$ structure and/or to destabilizing the IL structure lies in the iron environment. In the hypothetical IL structure of $(Sr_{0.2}Ba_{0.8})FeO_2$, the BVS of the iron ion is +1.81, which is smaller than the ideal value. This means that the Fe−O bond length now becomes too long to adopt the ideal square planar coordination. In the real structure of $(Sr_{0.2}Ba_{0.8})FeO_2$, the average BVS of iron in planar coordination is +2.23 for Fe(2) and +2.3 for Fe(3), implying that underbonding for the A site is less critical than for the Fe site. Note that the BVS of iron in the solubility limit for the IL phase, $(Sr_{0.7}Ba_{0.3})FeO_2$, is +1.93,[29] further reinforcing our discussion.

Apparently, the $BaFeO_2$ structure is structurally related to $LaNiO_{2.5}$ comprising one-dimensional octahedral chains linked by square planar units (Figure 1c), but there exist several important differences. First, the stability of the oxygen defect ordered structure of $LaNiO_{2.5}$ with two different Ni coordination geometries is brought by appropriate spin configurations; the high-spin state ($S = 1$) for the octahedral site and the low-spin state ($S = 0$) for the square planar site.[20] However, in the $BaFeO_2$ structure, all the iron ions are divalent and in a high-spin state ($S = 2$). Note also that $(La,Sr)CuO_2$, consisting of an ordered polyhedral network with 2-, 4-, and 5-fold coordination, has Cu in correspondingly different valence states, +1 and +2.[31]

Another crucial difference concerns the connectivity of the octahedral chains. The planar Fe(2) site is either 3- or 4-fold coordinated, resulting from the oxygen vacancies at O(2). More importantly, the significant oxygen deficiency at O(2) and O(4) around the otherwise octahedral Fe(3) site makes the average coordination number 3.56, a value close to that in the planar Fe(2) site. Thus it would be, in reality, inappropriate to consider Fe(3) as an octahedral site. The $BaFeO_2$ structure could be better described as a pillarlike structure with the Fe(1) octahedral chains bridged loosely by other lower coordination polyhedra.

The $Fe(1)O_6$ chain−chain distance is rather long, at ~8 Å ($2a_p$). Therefore, why such a loose framework is formed is an interesting question. The Fe(3) atom has a quite disordered coordination geometry with oxygen vacancies and is connected only by low-coordinate Fe(2) and Fe(3) atoms, along [100] and [001], respectively. The oxygen vacancies result in a random distribution of disconnected Fe(3)−(O)−Fe(3) and Fe(3)−(O)−Fe(2) bonds. Thus, this iron site will not play a crucial role for the stabilization of the loose framework, although Fe(2) and Fe(3) are covalently bonded, resulting presumably from planar coordination geometries as mentioned earlier. What would be essential is the full occupation for the O(1) and O(3) sites, which provides a rigid 3D connection of [−Fe(1)−O(3)−] along the $c$ axis and [−Fe(1)−O(1)−Fe(2)−O(1)−] along the $a$ ($b$) axis (Figure 6S, Supporting Information). Depending on the oxygen occupancy at the O(2) site, Fe(2) adopts square planar or trigonal coordination, but in each case it is connected by two neighboring $Fe(1)O_6$ octahedra. In other words, the Fe(2)−O(2) bonds give a firm link with the Fe(1) chains. A similar situation is found in a triple-layered perovskite, $Sr_3LaFe_{1.5}Co_{1.5}O_{7.5}$, where the inner perovskite layer, sandwiched by outer $BO_5$ pyramidal layers, consists of 68% $BO_3$ trigonal coordination (B = Fe/Co) with a significant degree of randomness.[43]

### 3.5. Physical Properties.

Both Mössbauer and neutron diffraction experiments revealed that $(Sr_{1-x}Ba_x)FeO_2$ ($x \geq 0.8$) is in a paramagnetic state at room temperature, in contrast to the IL structure with $T_N$ far beyond room temperature. When the temperature was decreased (Figure 7a), magnetic

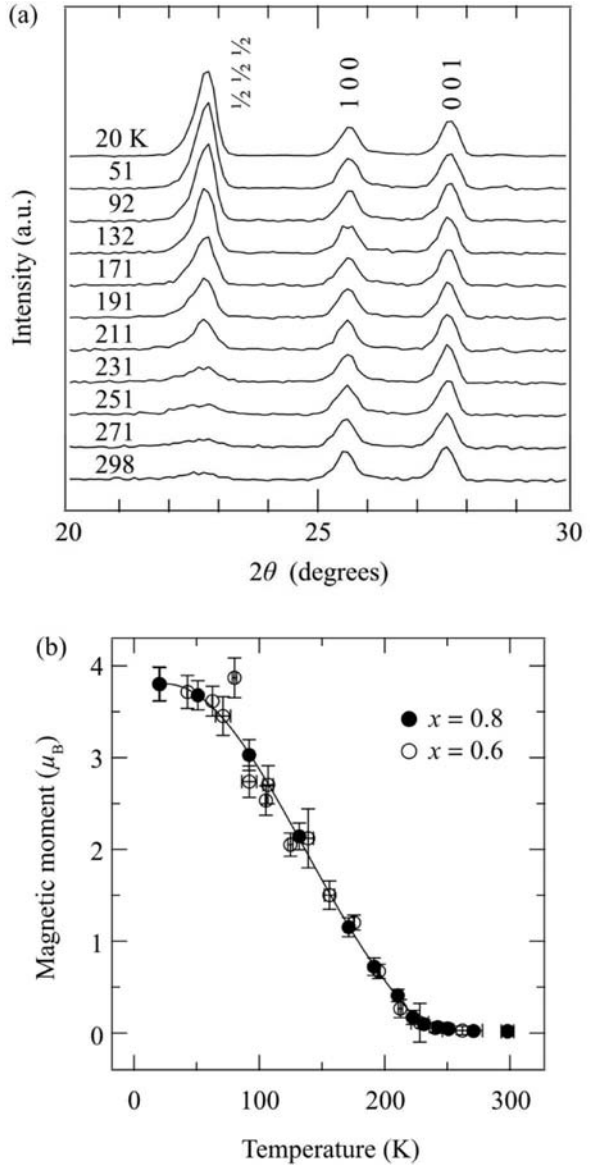

**Figure 7.** (a) Temperature evolution of the neutron diffraction profile for $x$ = 0.8 showing the magnetic Bragg reflection $(1/2,1/2,1/2)_p$, together with the nuclear Bragg reflections $(100)_p$ and $(001)_p$. (b) Temperature dependence of the magnetic moment in $(Sr_{1-x}Ba_x)FeO_2$ for $x$ = 0.6 (open) and 0.8 (closed). The Néel temperature ($T_N$) for both $x$ = 0.6 and $x$ = 0.8 compounds is determined to be about 240 K. The solid line is a guide to the eyes.

reflections were observed together with nuclear reflections. Neutron data revealed a *G*-type spin order, which is the same magnetic structure as the IL phase. The temperature dependence of the neutron diffraction pattern in Figure 7b shows that $T_N$ is about 240 K. From the Rietveld analysis for the $x$ = 0.8 data at 20 K, the magnetic moments of all the irons, Fe(1), Fe(2) (Fe(2)′), and Fe(3), are 3.8 $\mu_B$/Fe in magnitude and align in the *ab* plane. Therefore, all the iron ions are in a divalent high-spin configuration, like the IL phase. The neutron diffraction pattern for $(Sr_{0.4}Ba_{0.6})FeO_2$ (Figure 7S, Supporting Information) also shows the same type of spin order and similar magnetic moments of 3.8 $\mu_B$ at 20 K for all the iron sites. The $T_N$ is determined to be 240 K, which is the same as that for $x$ = 0.8. These observations indicate that the $x$ dependence of the magnetic properties is subtle, despite a non-negligible evolution of the lattice parameters.

The observed transition temperature of 240 K for $x$ = 0.6 and 0.8 is much lower than those for $SrFeO_2$ ($T_N$ = 473 K)[26] and $CaFeO_2$ ($T_N$ = 420 K).[31] The reduction in $T_N$ would result not only from the elongated iron−iron distance (along all the crystallographic directions) but also from the random oxygen deficiencies that break many Fe(2)−O(2)−Fe(3) and Fe(3)−O(4)−Fe(3) superexchange pathways. However, a closer look at the neutron diffraction patterns (Figure 7a) revealed that above $T_N$ weak but broad magnetic peaks persist, even at room temperature. No sign of splitting or broadening of the doublets was seen in the room temperature Mössbauer spectrum. This suggests that a short-range magnetic correlation is already developed at temperatures well beyond $T_N$, but magnetic fluctuations should be faster than the Mössbauer time window ($>10^{-8}$ s). It is also interesting to compare the magnetic properties of our system with those of $LaNiO_{2.5}$. Because of the high-spin ($S$ = 1) and low-spin ($S$ = 0) configurations at the octahedral and square planar sites, the magnetic property of this nickelate is best characterized by quasi one-dimensional $S$ = 1 chains made up of corner-shared $NiO_6$ octahedra along the *c* axis. Namely, although $Ni^{2+}$ ions are connected in the *ab* plane, the square planar site acts as a nonmagnetic separator, and as a result the magnetic order occurs at a rather low temperature ($T_N$ = 80 K).[20]

A trivalent lanthanum-substituted $BaFeO_2$ (**I**) was successfully obtained from the precursor $(Ba_{0.8}La_{0.2})FeO_{3-\delta}$ ($\delta < 0.5$). The XRD pattern of **I** could be indexed in the same tetragonal unit cell as $BaFeO_2$ (Figure 8a), and the lattice parameters ($a$ = 8.268 Å and $c$ = 3.846 Å) are slightly smaller than $a$ = 8.375 Å and $c$ = 3.879 Å in $BaFeO_2$. Super-reflections corresponding to the $2a_p \times 2a_p \times c_p$ cell are present. These facts indicate that **I** is isostructural with $BaFeO_2$. Because **I** is air sensitive and easily oxidized back to $(Ba_{0.8}La_{0.2})FeO_{3-\delta}$, the Mössbauer spectrum of **I** includes very broad peaks possibly arising from oxidized $(Ba_{0.8}La_{0.2})FeO_{3-\delta}$, as shown in Figure 8b. Nevertheless, ignoring this broad background, we were able to fit the spectrum well, as summarized in Figure 8b and Table 3S in the Supporting Information. All the fitted parameters of the subspectra are similar to those of $(Sr_{1-x}Ba_x)FeO_2$ ($x \geq 0.4$), suggesting that all the iron ions in **I** are in environments similar to those in $(Sr_{1-x}Ba_x)FeO_2$ ($x \geq 0.4$), all the iron sites being divalent and in the high-spin state. To account for this, the chemical formula must be $(Ba_{0.8}La_{0.2})FeO_{2.1}$. Here, the excess oxygen may occupy the vacant sites at O(2) and O(4) such that the iron valence state of +2 remains unaltered. In general, for a given (fixed) $y$, the reduced phase has a defined composition of $(Ba_{1-y}La_y)FeO_{2+y/2}$.

This compensated composition of $(Ba_{0.8}La_{0.2})FeO_{2.1}$ implies, in part, a failure of electron doping by the La-for-Sr substitution. Nevertheless, as shown in Figure 8c, the electrical resistance $\rho$ is measurable, in contrast to that of $(Sr_{1-x}Ba_x)FeO_2$ ($0 \leq x \leq 1$). The resistivity for $SrFeO_2$ is out of range of our experimental system and only becomes measurable when pressurized above 15 GPa.[35] The room temperature resistivity of **I** is high in magnitude (∼MΩ cm) and shows a semiconducting behavior with an activation energy of 0.21 eV. Note that a small amount of the amorphous impurity phase can be found in the Mössbauer spectrum. At this point, we cannot totally exclude the possibility that the impurity phase accounts for the resistivity decrease. However, since the amount of impurity estimated from Mössbauer data is comparable to

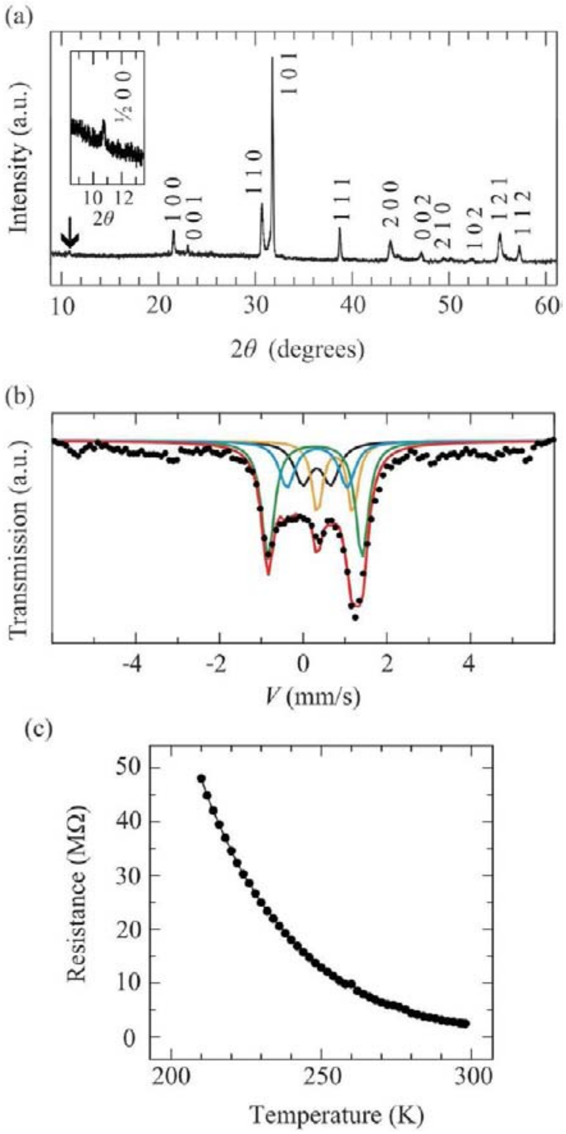

**Figure 8.** (a) XRD patterns of $(Ba_{0.8}La_{0.2})FeO_{2+\delta}$ collected in our laboratory. It could be indexed by a tetragonal system with lattice parameters $a$ = 8.268 Å and $c$ = 3.846 Å. (b) Mössbauer spectrum for $(Ba_{0.8}La_{0.2})FeO_{2+\delta}$ at room temperature. Circles denote the experimental data. The spectrum was fitted by four parameters; yellow, green, and blue lines represent spectra from Fe(1), Fe(2), and Fe(3) in $(Ba_{0.8}La_{0.2})FeO_{2+\delta}$, respectively. The black line represents an over-reduced, decomposed impurity formed during the hydride reaction. The red line represents the total of the four components. (c) Temperature dependence of the resistance.

that of $(Sr_{1-x}Ba_x)FeO_2$ ($0.4 \leq x \leq 1.0$), the lanthanum substitution plus additional oxygen insertion might result in a large change in the electronic structure with a reduced band gap. Theoretical investigation is needed for further understanding of the La-substitution effect on the electronic and physical properties.

## 4. CONCLUSION

$(Sr_{1-x}Ba_x)FeO_2$ ($0.4 \leq x \leq 1.0$) with a novel perovskite-related structure was successfully obtained by low-temperature topotactic reaction with calcium hydride ($0.4 \leq x \leq 0.9$) and sodium hydride ($x = 1.0$). The new structure is partly analogous to the $LaNiO_{2.5}$ structure with one-dimensional chains of octahedra linked by planar units, but differs in that one of the octahedral sites has a significant amount of oxygen vacancies and that all the iron ions have the same spin and valence state. Unlike recently reported iron oxides with square planar coordination, this structure demonstrates the ability of the iron square planar coordination to coexist with other types of coordination. Thus, it is expected that a large family of square planar based iron oxides will be prepared in the future. The Mössbauer spectra indicate that the Fe(2) and Fe(3) ions have extremely strong covalency, and this may contribute to the formation of the unique structure. At the same time, the rigidity of a 3D Fe−O−Fe connection which consists of [−Fe(1)−O(3)−] along the $c$ axis and [−Fe(1)−O(1)−Fe(2)−O(1)−] along the $a$ ($b$) axis acts to strengthen the framework. The extreme covalency of planar coordinate iron and its preferential valence (+2) stabilize this compound as a line phase with a defined composition, despite the presence of structural disorders and partial occupations.

The structural conversion between $BaFeO_2$ and $BaFeO_{2.5}$ involves a complex rearrangement of the oxygen framework at low temperature. The recent work on $CaFeO_{2.5}$−$CaFeO_2$ thin films[50] revealed different oxygen migration pathways with selective kinetics. Revealing the reaction mechanism (pathway) between $BaFeO_2$ and $BaFeO_{2.5}$ will also be an important subject for future study. We also obtained the La-substituted $BaFeO_2$ and showed that the additional oxygen atoms are incorporated into the structure. The importance of interstitial oxide ions has been recently stressed for the design of oxygen ion conductors.[51−54] The $BaFeO_2$ structure is hence interesting in connection with oxygen ion conductivity.

## ■ ASSOCIATED CONTENT

### Ⓢ Supporting Information

Supporting graphics, tables, and CIF data. This material is available free of charge via the Internet at http://pubs.acs.org.

## ■ AUTHOR INFORMATION

### Corresponding Author

kage@scl.kyoto-u.ac.jp

### Notes

The authors declare no competing financial interest.

## ■ ACKNOWLEDGMENTS

We thank Yoshihiro Tsujimoto and Takashi Watanabe for helpful discussions, Kenichi Kato and Jungeun Kim for support of the synchrotron X-ray diffraction experiments, Kenji Nemoto for support of the neutron powder diffraction experiments, and Kazuyoshi Kanamori for support of the thermogravimetric measurements. This work was supported by a Grant-in-Aid for Scientific Research (A) (22245009) from the Ministry of Education, Culture, Sports, Science and Technology of Japan, by the Japan Science and Technology Agency, CREST, and by the Global COE program International Center Science, Kyoto University, Japan. T.Y. was supported by the Japan Society for the Promotion of Science for Young Scientists.

## ■ REFERENCES

(1) Von Helmolt, R.; Wecker, J.; Holzapfel, B.; Schultz, L.; Samwer, K. *Phys. Rev. Lett.* **1993**, *71*, 2331−2333.

(2) Moritomo, Y.; Asamitsu, A.; Kuwahara, H.; Tokura, Y. *Nature* **1996**, *380*, 141−144.

(3) Jin, S.; Tiefel, T. H.; McCormack, M.; Fastnacht, R. A.; Ramesh, R.; Chen, L. H. *Science* **1994**, *264*, 413−415.

(4) Cohen, R. E. *Nature* **1992**, *358*, 136−138.
(5) Lacorre, P.; Torrance, J. B.; Pannetier, J.; Nazzal, A. I.; Wang, P. W.; Huang, T. C. *J. Solid State Chem.* **1991**, *91*, 225−237.
(6) Alonso, J. A.; Martínez-Lope, M. J.; Casais, M. T.; Aranda, M. A. G.; Fernández-Díaz, M. T. *J. Am. Chem. Soc.* **1999**, *121*, 4754−4762.
(7) Takano, M.; Nasu, S.; Abe, T.; Yamamoto, K.; Endo, S.; Takeda, Y.; Goodenough, J. B. *Phys. Rev. Lett.* **1991**, *67*, 3267−3270.
(8) Johnston, D. C.; Prakash, H.; Zachariasen, W. H.; Viswanathan, R. *Mater. Res. Bull.* **1973**, *8*, 777−784.
(9) Isobe, M.; Ueda, Y. *J. Phys. Soc. Jpn.* **2002**, *71*, 1848−1851.
(10) Nishizawa, M.; Ise, T.; Koshika, H.; Itoh, T.; Uchida, I. *Chem. Mater.* **2000**, *12*, 1367−1371.
(11) Schooley, J. F.; Hosler, W. R.; Cohen, M. L. *Phys. Rev. Lett.* **1964**, *12*, 474−475.
(12) Matsumoto, H.; Furya, Y.; Okada, S.; Tanji, T.; Ishihara, T. *Electrochem. Solid-State Lett.* **2007**, *10*, 11−13.
(13) Abrahams, E.; Kotliar, G. *Science* **1996**, *274*, 1853−1854.
(14) Hodges, J. P.; Short, S.; Jorgensen, J. D.; Xiong, X.; Dabrowski, B.; Mini, S. M.; Kimball, C. W. *J. Solid State Chem.* **2000**, *151*, 190−209.
(15) Ueda, Y.; Nakayama, N. *Solid State Ionics* **1998**, *108*, 303−306.
(16) Akahoshi, D.; Ueda, Y. *J. Solid State Chem.* **2001**, *156*, 355−363.
(17) Suescun, L.; Chmaissem, O.; Mais, J.; Dabrowski, B.; Jorgensen, J. D. *J. Solid State Chem.* **2007**, *180*, 1698−1707.
(18) Le Toquin, R.; Paulus, W.; Cousson, A.; Prestipino, C.; Lamberti, C. *J. Am. Chem. Soc.* **2006**, *128*, 13161−13174.
(19) Alonso, J. A.; Martínez-Lope, M. J.; García-Muñoz, J. L.; Fernández, M. T. *Physica B* **1997**, *234*, 18−19.
(20) Alonso, J. A.; Martínez-Lope, M. J.; García-Muñoz, J. L.; Fernández-Díaz, M. T. *J. Phys.: Condens. Matter* **1997**, *9*, 6417−6426.
(21) Vogt, T.; Leonowicz, M. E.; Longo, J. M. *J. Solid State Chem.* **1982**, *44*, 89−98.
(22) Poeppelmeier, K. R.; Woodward, P. M.; Karen, P.; Hunter, B. A.; Henning, P.; Moodenbaugh, A. R. *Phys. Rev. Lett.* **2000**, *84*, 2969−2972.
(23) Zou, X. D.; Hovmöller, S.; Parras, M.; González-Calbet, J. M.; Vallet-Regí, M.; Grenier, J. C. *Acta Crystallogr.* **1993**, *A49*, 27−35.
(24) Takano, M.; Takeda, Y.; Okada, H.; Miyamoto, M.; Kusaka, T. *Physica C* **1989**, *159*, 375−378.
(25) Crespin, M.; Levitz, P.; Gatineau, L. *J. Chem. Soc. Faraday Trans.* **1983**, *79*, 1181−1194.
(26) Tsujimoto, Y.; Tassel, C.; Hayashi, N.; Watanabe, T.; Kageyama, H.; Yoshimura, K.; Takano, M.; Ceretti, M.; Ritter, C.; Paulus, W. *Nature* **2007**, *450*, 1062−1065.
(27) Ikeda, N.; Hiroi, Z.; Azuma, M.; Takano, M.; Bando, Y.; Takeda, Y. *Physica C* **1993**, *210*, 367−372.
(28) Smith, M. G.; Manthiram, A.; Zhou, J.; Goodenough, J. B.; Markert, J. T. *Nature* **1991**, *351*, 549−551.
(29) Yamamoto, T.; Li, Z.; Tassel, C.; Hayashi, N.; Takano, M.; Isobe, M.; Ueda, Y.; Ohoyama, K.; Yoshimura, K.; Kobayashi, Y.; Kageyama, H. *Inorg. Chem.* **2010**, *49*, 5957−5962.
(30) Tassel, C.; Watanabe, T.; Tsujimoto, Y.; Hayashi, N.; Kitada, A.; Sumida, Y.; Yamamoto, T.; Kageyama, H.; Takano, M.; Yoshimura, K. *J. Am. Chem. Soc.* **2008**, *130*, 3764−3765.
(31) Tassel, C.; Pruneda, J. M.; Hayashi, N.; Watanabe, T.; Kitada, A.; Tsujimoto, Y.; Kageyama, H.; Yoshimura, K.; Takano, M.; Nishi, M.; Ohoyama, K.; Mizumaki, M.; Kawamura, N.; Íñiguez, J.; Canadell, E. *J. Am. Chem. Soc.* **2009**, *131*, 221−229.
(32) Otzschi, K.; Koga, K.; Ueda, Y. *J. Solid State Chem.* **1995**, *115*, 490−498.
(33) Kageyama, H.; Watanabe, T.; Tsujimoto, Y.; Kitada, A.; Sumida, Y.; Kanamori, K.; Yoshimura, K.; Hayashi, N.; Muranaka, S.; Takano, M.; Ceretti, M.; Paulus, W.; Ritter, C.; André, G. *Angew. Chem., Int. Ed.* **2008**, *47*, 5740−5745.
(34) Dixon, E.; Hayward, M. A. *Inorg. Chem.* **2010**, *49*, 9649−9654.
(35) Kawakami, T.; Tsujimoto, Y.; Kageyama, H.; Chen, X. Q.; Fu, C. L.; Tassel, C.; Kitada, A.; Suto, S.; Hirama, K.; Sekiya, Y.; Makino, Y.; Okada, T.; Yagi, T.; Hayashi, N.; Yoshimura, K.; Nasu, S.; Podloucky, R.; Takano, M. *Nat. Chem.* **2009**, *1*, 371−376.
(36) Yamamoto, T.; Tassel, C.; Kobayashi, Y.; Kawakami, T.; Okada, T.; Yagi, T.; Yoshida, H.; Kamatani, T.; Watanabe, Y.; Kikegawa, T.; Takano, M.; Yoshimura, K.; Kageyama, H. *J. Am. Chem. Soc.* **2011**, *133*, 6036−6043.
(37) Tamura, R.; Kawashima, N.; Yamamoto, T.; Tassel, C.; Kageyama, H. *Phys. Rev. B* **2011**, *84*, 214408.
(38) Seinberg, L.; Yamamoto, T.; Tassel, C.; Kobayashi, Y.; Hayashi, N.; Kitada, A.; Sumida, Y.; Watanabe, T.; Nishi, M.; Ohoyama, K.; Yoshimura, K.; Takano, M.; Paulus, W.; Kageyama, H. *Inorg. Chem.* **2011**, *50*, 3988−3995.
(39) Hayward, M.; Green, M.; Rosseinsky, M.; Sloan, J. *J. Am. Chem. Soc.* **1999**, *121*, 8843−8854.
(40) Hayward, M.; Cussen, E.; Claridge, J.; Bieringer, M.; Rosseinsky, M.; Kiely, C.; Blundell, S.; Marshall, I.; Pratt, F. *Science* **2002**, *295*, 1882−1884.
(41) Poltavets, V. V.; Lokshin, K. A.; Dikmen, S.; Croft, M.; Egami, T.; Greenblatt, M. *J. Am. Chem. Soc.* **2006**, *128*, 9050−9051.
(42) Seddon, J.; Suard, E.; Hayward, M. A. *J. Am. Chem. Soc.* **2010**, *132*, 2802−2810.
(43) Bowman, A.; Allix, M.; Pelloquin, D.; Rosseinsky, M. J. *J. Am. Chem. Soc.* **2006**, *128*, 12606−12607.
(44) Morimoto, S.; Kuzushita, K.; Nasu, S. *J. Magn. Magn. Mater.* **2004**, *272−276*, 127−129.
(45) Ohoyama, K.; Kanouchi, T.; Nemoto, K.; Ohashi, M.; Kajitani, T.; Yamaguchi, Y. *Jpn. J. Appl. Phys.* **1998**, *37*, 3319−3326.
(46) Izumi, F.; Momma, K. *Solid State Phenom.* **2007**, *130*, 15−20.
(47) Brown, I. D.; Altermatt, D. *Acta Crystallogr.* **1985**, *B41*, 244−247.
(48) Greenwood, N. N.; Gibb, T. C. *Mössbauer Spectroscopy*; Chapman and Hall: London, 1971.
(49) Yang, M.; Oró-Solé, J.; Rodgers, J. A.; Jorge, A. B.; Fuertes, A.; Attfield, J. P. *Nat. Chem.* **2010**, *3*, 47−52.
(50) Inoue, S.; Kawai, M.; Ichikawa, N.; Kageyama, H.; Paulus, W.; Shimakawa, Y. *Nat. Chem.* **2010**, *2*, 213−217.
(51) Boehm, E.; Bassat, J. M.; Steil, M. C.; Dordor, P.; Mauvy, F.; Grenier, J. C. *Solid State Sci.* **2003**, *5*, 973−981.
(52) Demourgues, A.; Wattiaux, A.; Grenier, J. C.; Pouchard, M.; Soubeyroux, J. L.; Dance, J. M.; Hagenmuller, P. *J. Solid State Chem.* **1993**, *105*, 458−468.
(53) Kuang, X.; Green, M. A.; Niu, H.; Zajdel, P.; Dickinson, C.; Claridge, J. B.; Jantsky, L.; Rosseinsky, M. J. *Nat. Mater.* **2008**, *7*, 498−504.
(54) Orera, A.; Slater, P. *Chem. Mater.* **2009**, *22*, 675−690.